

Electrically driven thermal light emission from individual single-walled carbon nanotubes

David Mann,¹ Y. K. Kato,¹ Anika Kinkhabwala,¹ Eric Pop,^{1,2} Jien Cao,¹ Xinran Wang,¹ Li Zhang,¹ Qian Wang,¹ Jing Guo,³ and Hongjie Dai^{1,*}

¹ Dept. Chemistry and Lab. Adv. Materials, Stanford Univ., Stanford, CA 94305, USA

² Intel Corp., Santa Clara, CA 95054, USA

³ Department of Electrical and Computer Engineering, Univ. Florida, Gainesville, FL, 32611

Journal reference: Nature Nanotechnology vol. 2, no. 1, pp. 33 – 38 (2006)

Light emission from nanostructures exhibits rich quantum effects and has broad applications. Single-walled carbon nanotubes (SWNTs) are one-dimensional (1D) metals or semiconductors, in which large number of electronic states in a narrow range of energies, known as van Hove singularities, can lead to strong spectral transitions.^{1,2} Photoluminescence and electroluminescence involving interband transitions and excitons have been observed in semiconducting SWNTs,³⁻⁹ but are not expected in metallic tubes due to non-radiative relaxations. Here, we show that in the negative differential conductance regime, a suspended quasi-metallic SWNT (QM-SWNT) emits light due to joule-heating, displaying strong peaks in the visible and infrared corresponding to interband transitions. This is a result of thermal light emission in 1D, in stark contrast with featureless blackbody-like emission observed in large bundles of SWNTs or multi-walled nanotubes.¹⁰⁻¹² This allows for probing of the electronic temperature and non-equilibrium hot optical phonons in joule-heated QM-SWNTs.

We investigated electrically driven thermal light emission of individual QM-SWNTs in both the visible and infrared (infrared) (wavelength $\lambda=500-2100$ nm, Supplementary Information), in a wider spectral window than previously explored for electroluminescence of nanotubes. We fabricated suspended and non-suspended SWNT (diameter $d\sim 2-4$ nm) devices with tube length $L \sim 2-10$ μm (Fig. 1a, 1c insets), as described previously.¹³⁻¹⁵ QM-SWNTs were identified as those exhibiting weak source-drain current (I_{ds}) dependence (due to small band-gaps \sim tens of meV^{14, 16}) on gate-voltage (V_{gs}) with $I_{ds}(max)/I_{ds}(min) < 10$ (at bias $V_{ds}=10$ mV), across the V_{gs} range (Fig. 1a). On substrate, QM-SWNTs show current saturation near 20 μA at high bias, while suspended ones exhibit negative differential conductance (i.e., reduced currents at higher biases) and much lower maximum current < 10 μA (Fig. 1b) due to joule-heating and electron scattering by hot optical phonons caused by slow heat dissipation in suspended SWNTs.¹⁵

We observed light emission from suspended QM-SWNTs (in on-state under a high negative V_{gs} , with the device kept in Ar) beginning at low V_{ds} , with pronounced peaks in the spectra (Fig. 1c, 2a&2b). We measured the visible emission characteristics of the suspended and on-substrate sections of several QM-SWNTs (Fig. 1c) and observed that the onset of detectable visible light for suspended QM-SWNT devices began as low as $V_{ds} = 0.9$ V (always in the negative differential conductance region in $I_{ds}-V_{ds}$ as the one in Fig. 1b), while the visible emission for on-substrate SWNTs was not measurable until $V_{ds} > 5$ V. For several long (10 μm) suspended QM-SWNTs, we spatially resolved light emission and found that the location of the brightest spot was always near the center (Fig. 1d) and remained stationary at various V_{ds} and V_{gs} .

We investigated light emission from ten suspended (all in Ar) QM-SWNTs (Fig. 2). All QM-SWNTs exhibited spectral peaks and the peak positions varied (Fig. 2a&2b). In SWNTs, electronic transitions between the van Hove singularities are dipole-allowed (denoted as E_{mn} transitions).¹⁷ We attribute the observed peaks to optical emission (highly polarized along

tube axis, Fig. 2b inset) from E_{11} (infrared) and E_{22} (visible or near infrared) transitions (Fig. 2c) of QM-SWNTs. Lorentzian fitting is used to determine the peak locations of E_{11} and E_{22} . We find reasonable agreement with simple tight-binding predicted E_{11} and E_{22} values ($\sim 1:2$ ratio) (Fig. 2d)¹⁸ for QM-SWNTs with $d \sim 2.8$ to 4nm (d was measured by atomic force microscopy over the on-substrate portion of the nanotubes).

To understand the light emission in QM-SWNTs, we note that the negative differential conductance in the $I_{ds}-V_{ds}$ of suspended QM-SWNTs is indicative of significant self-heating and electron scattering by hot optical phonons.¹⁵ The slow decay and long lifetimes of optical phonons in suspended SWNTs lead to high non-equilibrium optical phonon population and temperature (T_{op}), causing significant electron heating ($T_e \sim T_{op}$) well above the temperature of the SWNT lattice.^{15, 19} Analysis of the negative differential conductance region of the $I_{ds}-V_{ds}$ curve of a $\sim 2\mu\text{m}$ suspended QM-SWNT by the hot phonon model^{15, 19} leads to an estimated $T_e \sim T_{op} \sim 1200$ K at $V_{ds} \sim 1.3$ V. This heating gives rise to a thermal distribution of electrons and holes with appreciable populations at the van Hove singularities in QM-SWNTs (Fig. 2c). These carriers can then radiatively recombine to produce E_{11} and E_{22} emission peaks, thus producing distinct spectral features rather than featureless blackbody spectrum. Note that excitons may play a role in metallic and QM-SWNTs, but the effect should be smaller in our case than in semiconducting-SWNTs due to large $d \sim 2\text{-}4\text{nm}$ QM-SWNTs used with low exciton binding energies²⁰ relative to the high T_e involved. The effect is difficult to discern from our spectra with broad peaks caused by significant heating.

This thermal light emission model is consistent with the observed emission photon energy exceeding the bias-voltage injection energy eV_{ds} (emission well above $eV_{ds}=1.4\text{eV}$ is seen in Fig. 1c). It is also consistent with the drastic difference in light emission between the suspended and on-substrate portions of a SWNT (Fig. 1c), since self-heating of the latter is much lower due to efficient thermal dissipation and optical phonons relaxation into the substrate.^{15, 21} In fact, in ambient air without the protection of Ar flow, our suspended

SWNTs breakdown at sustained biases $V_{ds} \sim 1.5-2V$ (see Supplementary Fig.S1) as a result of oxidation as their lattice temperature approaches $\sim 800K$.²² The thermal light emission model is further consistent with the fact that light emission is brightest at the center of the suspended QM-SWNTs (Fig.1d) where a parabolic temperature profile peaks.¹⁵ This differs from previous spatially resolved electroluminescence in semiconducting-SWNTs in which emission was observed at the suspended trench edge attributed to impact excitation and exciton recombination⁷, and the mobile emission spot seen as a result of ambipolar carrier injection.⁵ We carried out theoretical modeling (see Method section) to fit the experimental spectra (Fig. 3a &3c) and extract electron temperatures by spectra fitting in the visible region, and the results are close to the optical phonon temperature ($T_e \sim T_{op}$) derived from the hot phonon model (Fig. 3b left axis).^{15, 19} Note that our model is mainly used to fit the exponential emission tail in the visible for extracting electron temperature, not intended to precisely fit the peak positions.

Several features in our spectra are not well understood. First, $E_{11}:E_{22} \sim 1:1.7-2$ has been observed for semiconducting-SWNTs by photoluminescence experiments.^{23, 24} In our case of QM-SWNT thermal light emission, in which we do not consider excitonic effects, we expect $E_{11}:E_{22} \sim 1:2$, but deviations from this ratio were observed (Fig.2d). One possible cause is significant heating effect on the nanotube structure and in turn electronic structure. Some of our QM-SWNTs exhibited unexplained peaks (e.g., in red curve of Fig. 2a) between E_{11} and E_{22} . Possibilities include phonon assisted transitions, inter-band transitions (e.g., E_{12} for which theoretical work has suggested perpendicular polarization and intensity up to a $\sim 1/5-1/3$ of E_{nn} transitions²⁵), and possibly emission from states due to defects along the relatively long tubes. These possibilities require further investigations. We calculated the effect of trigonal warping²⁶ on our spectra and found the effect to be inconsequential in this diameter range ($d \sim 2.8-4nm$), given the breadth of the measured emission peaks ($>100meV$).

For the SWNT in Fig. 3c, we have analyzed the peak width (full-width half maximum $\sigma \sim 130$ meV) as a function of bias by fitting several spectra ($V_{ds} = 0.7$ to 1.2V). As V_{ds} and thus T_e increases, the emission peak is expected to widen from increased thermal and lifetime broadening effects. Indeed, we observed peak-width change over the bias range (Fig. 3c). The apparent peak-widths correspond to effective lifetimes of $\tau_{TOT} \sim 10$ to 14 fs, including all scattering mechanisms (Fig. 3d left axis). By using the calculated T_{op} (and the corresponding Bose-Einstein optical phonon occupation number) from the hot phonon model,^{15, 19} we determined an electron-phonon scattering lifetime of $\tau_{e-op} \sim 15$ to 18 fs (Fig. 3d right axis), about 50% greater than τ_{TOT} . This suggests that only a portion of τ_{TOT} is due to electron-phonon scattering, with additional broadening likely due to other mechanisms, such as electron-electron scattering.

Lastly, we carried out light emission measurements of QM-SWNTs as a function of bias V_{ds} and gate-voltage V_{gs} (Fig. 4). At a fixed bias V_{ds} , the infrared light emission γ (down to 0.57eV) under various V_{gs} scaled exponentially with current or power ($P = I_{ds}V_{ds}$) (Fig. 4a), since increases in the latter caused higher T_e . Current modulation by V_{gs} (Fig. 4b, also Fig. 1a) was due to the existence of small band-gaps (\sim tens of meV) in the QM-SWNTs.¹³⁻¹⁶ By simultaneously measuring light emission γ and power P vs. V_{ds} and V_{gs} (Fig. 4c and 4d respectively), we observed that the exponential dependence of γ on P held across the entire V_{gs} and V_{ds} two-dimensional space.

Figure 4a has striking similarities to the data presented previously.⁷ While Chen et al. attribute this to impact excitation and recombination of free carriers and excitons,⁷ we rule out impact excitation as cause of light emission in our devices due to the observation of photons of greater energy than the applied field ($E_{photon} > eV_{ds}$) (Fig. 1c red curve and Fig. 3a). Additionally, we do not expect appreciable light emission from impact excitation as a result of non-radiative relaxation of excited carriers in QM-SWNTs.²⁰ We have also measured light emission of suspended semiconducting-SWNTs and found that thermal effects also occur in

semiconducting tubes (See Supplementary Fig.S2). The data suggests that thermal heating may play a role in other electroluminescence measurements of semiconducting-SWNTs,³⁻⁹ where similar or higher powers than that reported here are dissipated in the devices.

Our measurement gleans the high temperature optoelectronic properties of quasi-metallic SWNTs. By exploiting SWNTs of specific diameters, one can produce thermal light emission peaked at desired wavelength from visible to infrared, which is useful for optoelectronics for telecommunications in 1.3-1.5 μm range. While thermal light emission of bulk materials has been extensively studied, our result revealing drastic spectra peaks for SWNTs underlines the importance of examining electronic heating and emission in novel nanomaterials.

METHODS

Experimental details:

Fabrication of devices, methods for ensuring single tubes, light emission spectra and spatially resolved emission and electrical measurements are described in Supplementary Information.

Theoretical modelling of thermal light emission spectra of QM-SWNTs:

We use the tight-binding approximation to calculate the approximate joint density of states $D_J(E) = D(E/2)/2$ (where E is the transition energy and D is the density of states)¹⁸ for a SWNT of a certain diameter d , and introduce broadening of the D_J by convolving it with a function B (either Gaussian or Lorentzian),²⁸

$$D_J^B(E) = \int_{-\infty}^{+\infty} dE' \cdot D_J(E') \cdot B(E - E', \sigma) \quad (1)$$

where σ is the broadening width (due to finite lifetime of carriers scattered by phonons and other mechanisms) and used as a fitting parameter. It is important to note that D_J does *not*

include the metallic electronic band, since the dipole transition matrix element is zero for that band.²⁹ As an approximation (without including exciton effects for the large diameter QM-SWNTs used in the current work), we calculated the emission spectrum by³⁰

$$S(E) = \frac{1}{\tau(E)} D_J(E) f_0[E_C(k) - F_n] \{1 - f_0[E_V(k) - F_p]\}, \quad (2)$$

where $S(E)$ is the photon count (\sim light intensity), $E = E_C(k) - E_V(k)$ is the emitted photon energy, $D_J(E)$ is the joint density-of-states, $f_0(E)$ is the Fermi-Dirac distribution at high T_e (resulting from self-heating) and $1/\tau(E)$ is the transition probability. $E_C(k) = -E_V(k)$ if the middle of the bandgap is defined as the energy zero because the conduction and valence bands of SWNTs are symmetric, and we assume that the electron and hole quasi-Fermi levels $F_n \approx F_p \approx 0$ under all experimental gate voltages because the nanotube is quasi-metallic and the gate efficiency factor is small (~ 0.01)¹³⁻¹⁵ (Fermi level modulation by gate voltages involved only leads to a variation of $< 20\%$ in the product of the electron and hole Fermi-Dirac population terms in Eq.(2).) The emission rate $\frac{1}{\tau(E)} = \frac{2\pi}{\hbar} \left(\frac{q}{m_0} p_{CV} A \right)^2 \left(\frac{2}{3} D_{ph}(E) \right)$ depends on the momentum matrix element p_{CV} , the magnitude of the vector potential A , and the photon density of states $D_{ph}(E)$, and we assume that it is energy-independent for simplicity.³⁰ For three-dimensional isotropic (black-body) photons, $D_{ph} \propto \omega^2 (E=h\omega)$, and $1/\tau(E) \sim p_{CV}^2 \omega \sim r_{CV}^2 \omega^3$, where the dipole matrix element $r_{CV} = p_{CV} / (im_0\omega)$ and i is the imaginary unit. In a quasi one-dimensional SWNT, the momentum matrix element p_{CV} slightly decreases with energy.³⁰ The energy dependence of the emission spectrum in Eq. (2) is then dominant by the Fermi-Dirac distribution terms in an exponential manner. From $\sim 1.2\text{eV}$ to 2.0eV in the visible range in which our model fitting is carried out for electron temperature extraction, $1/\tau(E)$ computed using $\sim p_{CV}^2 \omega$ varies by a factor of < 2 , but the product of the Fermi-Dirac distribution terms varies by more than 4 orders of magnitude at $T_e = 1000\text{K}$.

Using our model with Gaussian broadening, we obtained excellent fitting of the experimental visible spectra (Fig. 3a) and were able to extract T_e at various V_{ds} (square symbols in Fig. 3b). The emission spectrum in the visible essentially exhibits an exponential decay ($\sim e^{-E/k_B T_e}$ due to the Fermi-Dirac distributions in Eq. 2) into the high energy end, with a superimposing hump at $\sim 1.6\text{eV}$ corresponding to the E_{22} transition (Fig. 3a). Thus the visible spectrum of suspended QM-SWNTs allows for an experimental determination of T_e ($\sim T_{op}$) for individual SWNTs under joule heating at various V_{ds} . Under higher V_{ds} , a suspended SWNT exhibits more Joule heating and higher T_e (Fig. 3b left axis), and thus an exponential increase in light emission (see bias dependent spectra in Fig. 3a&3c, and Fig. 3b right axis). Importantly, we found that the extracted T_e (squares in Fig. 3b) from emission spectra agree well with those obtained (Fig. 3b blue line) by fitting I_{ds} - V_{ds} curves (Fig. 3b inset) using the hot phonon model.^{15, 19}

The emission spectra of suspended QM-SWNTs in the lower energy infrared regime were dominated by the E_{11} peak (Fig. 2a&3c). This supports our assumption for the model where the transitions within the metallic band are forbidden,²⁹ since otherwise an exponentially increasing emission would exist on the lower energy side of the E_{11} peak. It is interesting that thermal light emission spectra gives insights to the magnitudes of the optical transition matrix elements, but this lack of an exponential slope causes difficulty in extracting T_e by spectra analysis in the infrared region. Instead, by using the calculated temperatures from the I_{ds} - V_{ds} fits, Lorentzian broadening and allowing only the width σ to vary (after fixing the other parameters by fitting one spectrum), we modelled the infrared spectra with excellent agreement with experiment for the SWNT in Fig. 3c. This agreement suggests that contrasting SWNT emission spectra in the infrared region with blackbody is not sufficient to exclude the possibility of thermal emission as done in a recent work.⁸ The total photon counts γ in the infrared (Fig. 3b red line) can be estimated as $\gamma(T_e) \sim Ae^{-E/k_B T_e}$ at various V_{ds} (and in turn various T_e) with $E \sim 0.8\text{eV} \sim E_{11}$ (photon energy of the peak in Fig. 3c), in agreement with the measured results (Fig. 3b red symbols).

FIGURE CAPTIONS

Figure 1. Visible thermal electroluminescence of quasi-metallic SWNTs. **(a)** Current vs. gate-voltage I_{ds} - V_{gs} curve for a 2 μm long suspended QM-SWNT device schematically shown in the inset (S: source; D: drain). **(b)** Current vs. bias I_{ds} - V_{ds} characteristics of the SWNT in (a) (showing negative difference conductance), together with that of the non-suspended portion of the same tube. **(c)** Visible emission spectra for the suspended and non-suspended portion of the QM-SWNT recorded at low and high bias V_{ds} , respectively ($V_{ds}=1.4\text{V}$, $I_{ds}=5\ \mu\text{A}$, and $V_{ds}=7\ \text{V}$, $I_{ds}=21\ \mu\text{A}$). Inset shows a scanning electron microscopy image (scale bar is 2 μm) of the device with suspended and on-substrate SWNT portions bridging electrodes. **(d)** Visible confocal image of a 10 μm suspended QM-SWNT at $V_{ds}=1.9\ \text{V}$ ($I \sim 3\ \mu\text{A}$) collected by silicon avalanche photo-detector superimposed on a dark-field optical image (the brightest horizontal lines mark the edge of the electrodes). The strongest light emission is seen at the center of the suspended tube (approximate location traced by the dashed line). Right panel: γ line-cut (total photon counts) along the tube length. The resolution of this measurement is nearly diffraction limited ($\sim 1\ \mu\text{m}$).

Figure 2. Thermal light emission of suspended metallic SWNTs with E_{11} and E_{22} peaks. **(a)** Light emission spectra (scaled for readability) in the infrared for three independent 2 μm long QM-SWNTs (red green and blue) at $V_{gs} = -20\text{V}$ and $V_{ds} = 1.4, 1.1, 1.3\ \text{V}$ respectively ($I_{ds}=6.35, 5.13, 5.95\ \mu\text{A}$). **(b)** Corresponding light emission spectra for the three tubes in (a) in the visible at $V_{gs} = -20\text{V}$ and $V_{ds} = 1.5, 1.3, 1.5\ \text{V}$ ($I_{ds}=6.15, 4.78, 5.7\ \mu\text{A}$) respectively. Inset: symbols are measured photon counts for emission polarized at various angles relative to tube axis. Solid line is a \cos^2 fit. **(c)** Illustration of thermal light emission mechanism in a $[m,n]=[24,21]$ QM-SWNT (with $d\sim 3\text{nm}$, $E_{11}\sim 0.8\text{eV}$, $E_{22}\sim 1.6\text{eV}$ as for the tube in a&b) with red curves). The curve on the blue region corresponds to electron population at various energies calculated by multiplying the density of states (black line) and the Fermi-Dirac distribution (red line) at $T_e\sim 1200\text{K}$. The finite populations at the first and second van Hove

singularities are responsible for E_{11} and E_{22} optical emission and depend on T_e and energy exponentially. **(d)** E_{11} vs. E_{22} peak locations from ten suspended QM-SWNT devices determined from their visible and infrared spectra. The red line corresponds to $E_{22} = 2E_{11}$ from the simple tight binding approximation. The peaks were determined using a Lorentzian curve fit. As a result, some of the devices showing asymmetric peaks had some offset due to imperfect fit.

Figure 3. Thermal light emission spectra of a 2.9 μm long suspended QM-SWNT compared with theory. **(a)** Visible spectra of a 2.9 μm long suspended QM-SWNT at two biases $V_{ds} = 1.2$ (blue) and 1.3 V (red) (top-panel). Lower panel shows spectra calculated for a $d \sim 3\text{nm}$ SWNT with $E_{11} \sim 0.8\text{eV}$ and $E_{22} \sim 1.6\text{eV}$ using Eq. 2. Several $d \sim 3\text{nm}$ SWNTs (e.g., [24,21] and [28,16]) have similar E_{11} and E_{22} , making it not possible to uniquely determine [m,n]. **(b)** Left axis: Electron temperature T_e ($\sim T_{op}$) vs. bias (blue line) derived by fitting $I_{ds}-V_{ds}$ data (symbols in inset) using the hot phonon model.^{15,19} Blue squares are T_e extracted from fitting visible thermal light emission spectra (see Method) in (a) for the two biases. Right axis: Measured γ vs. bias in the infrared region (red symbols) and computed γ (red line) based on T_e derived from the $I_{ds}-V_{ds}$ model.^{15,19} **(c)** Thermal light emission spectra in the infrared region for the SWNT at $V_{ds} = 0.7$ (black), 0.8 (green), 1.0 (blue) and 1.2 V (red) (top panel). Lower panel is calculated spectra using Eq. 2 and T_e at corresponding biases from (b). Note that a more precise theoretical treatment should include any exciton effects in our $d \sim 2\text{-}4\text{nm}$ QM-SWNTs. The exciton binding energies for large diameter QM-SWNTs are unknown but should be smaller than $\sim 80\text{meV}$ theoretically expected for a $d \sim 0.5\text{nm}$ QM-SWNT.²⁷ The effect may cause a shift in the emission peak positions, but the shift will be small compared to the large thermal light emission peak width ($\sim 130\text{meV}$). **(d)** Left axis: estimated hot-electron lifetime (τ_{TOT}) at various biases. Right axis: calculated electron- optical phonon scattering time at various biases at corresponding temperatures obtained from $I_{ds}-V_{ds}$ analysis.

Figure 4. Thermal light emission of suspended QM-SWNTs exhibits exponential dependence on power dissipation in the devices. **(a)** Total power dissipation $P(=I_{ds}V_{ds})$ vs. V_{gs} for a typical QM-SWNT device at $V_{ds} = 1$ V (black line, left axis in linear scale) and corresponding emission (total photon count in *log* scale) vs. V_{gs} in the infrared (red line, right axis). The electrical contact resistance is always an order of magnitude less than the suspended SWNT resistance at high bias. Power dissipation due to contact resistance was not excluded from P . **(b)** I_{ds} map (color scale bar on top) at various V_{ds} and V_{gs} showing the evolution of I_{ds} - V_{ds} versus V_{gs} . **(c)** Thermal light emission (γ) map (top: color scale in *log*) in the infrared region at various V_{ds} and V_{gs} . **(d)** power dissipation map P (top: color scale bar in linear scale) calculated by $P=I_{ds}V_{ds}$ from (b) at various V_{ds} and V_{gs} . The close resemblance between the thermal light emission map in *log* scale and power dissipation map in linear scale strongly suggests that light emission scales exponentially with power and supports the thermal light emission model.

Acknowledgements

We thank Professor W.E. Moerner for use of the confocal optical setup. This work was supported in part by MARCO MSD Focus Center and a NSF-NIRT.

H.D., D. M. and Y.K. conceived and designed the experiments. D.M., Y.K., A.K., E.P., J.C, X.W., L.Z., Q.W., J.G. performed the experiments and analyzed data. H.D., D.M. and Y.K. co-wrote the manuscript.

All authors discussed the results and commented on the manuscript.

* Correspondence and request for materials should be addressed to HD, hdai@stanford.edu

Competing financial interests

The authors declare that they have no competing financial interests

References

1. Dresselhaus, M. & Dai, H. (eds.) MRS 2004 Carbon Nanotube Special Issue, Vol. 29. (2004).
2. Saito, R., Fujita, M., Dresselhaus, G. & Dresselhaus, M.S. Electronic structure of graphene tubules based on C₆₀. *Phys. Rev. B* **46**, 1804 (1992).
3. O'Connell, M.J. et al. Band gap fluorescence from individual single-walled carbon nanotubes. *Science* **297**, 593-596 (2002).
4. Lefebvre, J., Homma, Y. & Finnie, P. Bright band gap photoluminescence from unprocessed single-walled carbon nanotubes. *Phys. Rev. Lett.* **90**, 217401 (2003).
5. Freitag, M. et al. Mobile ambipolar domain in carbon-nanotube infrared emitters. *Phys. Rev. Lett.* **93**, 076803 (2004).
6. Freitag, M. et al. Hot carrier electroluminescence from a single carbon nanotube. *Nano Lett.* **4**, 1063 (2004).
7. Chen, J. et al. Bright infrared emission from electrically induced excitons in carbon nanotubes. *Science* **310**, 1171 (2005).
8. Marty, L. et al. Exciton formation and annihilation during 1D impact excitation of carbon nanotubes. *Phys. Rev. Lett.* **96**, 136803 (2006).
9. Misewich, J.A. et al. Electrically induced optical emission from a carbon nanotube FET. *Science* **300**, 783 (2003).
10. Sveningsson, M., Jonsson, M., Nerushev, O.A., Rohmund, F. & Campbell, E.E.B. Blackbody radiation from resistively heated multiwalled carbon nanotubes during field emission. *Appl. Phys. Lett.* **81**, 1095 (2002).
11. Wei, J.Q., Zhu, H.W., Wu, D.H. & Wei, B.Q. Carbon nanotube filaments in household light bulbs. *Appl. Phys. Lett.* **84**, 4869 (2004).
12. Li, P. et al. Polarized incandescent light emission from carbon nanotubes. *Appl. Phys. Lett.* **82**, 1763 (2003).
13. Cao, H., Wang, Q., Wang, D.W. & Dai, H.J. Suspended carbon nanotube quantum wires with two gates. *Small* **1**, 138 (2005).
14. Cao, J., Wang, Q. & Dai, H. Electron transport in very clean, as-grown suspended carbon nanotubes. *Nat. Mat.* **4**, 745 (2005).
15. Pop, E. et al. Negative differential conductance and hot phonons in suspended nanotube molecular wires. *Phys. Rev. Lett.* **95**, 155505-155508 (2005).
16. Zhou, C., Kong, J. & Dai, H. Intrinsic electrical properties of single-walled carbon nanotubes with small band gaps. *Phys. Rev. Lett.* **84**, 5604 (2000).
17. Ichida, M. et al. Coulomb effects on the fundamental optical transition in semiconducting single-walled carbon nanotubes: Divergent behavior in the small-diameter limit. *Phys. Rev. B* **65**, 241407 (2002).
18. Mintmire, J.W. & White, C.T. Universal density of states for carbon nanotubes. *Phys. Rev. Lett.* **81**, 2506-2509 (1998).
19. Mann, D. et al. Thermally and molecularly stimulated relaxation of hot phonons in suspended carbon nanotubes. *J. Phys. Chem. B* **110**, 1502-1505 (2006).
20. Ando, T. Excitons in Carbon Nanotubes. *J. Phys. Soc. Japan* **66**, 1066-1073 (1997).
21. Pop, E., Mann, D., Reifenberg, J., Goodson, K.E. & Dai, H.J. in Intl. Electron Devices Meeting (IEDM) 253-256 Washington, DC; 2005).
22. Hata, K. et al. Water-Assisted Highly Efficient Synthesis of Impurity-Free Single-Walled Carbon Nanotubes. *Science* **306**, 1362-1364 (2004).

23. Bachilo, S.M. et al. Structure-assigned optical spectra of single-walled carbon nanotubes. *Science* **298**, 2361-2236 (2002).
24. Weisman, R.B. & Bachilo, S.M. Dependence of Optical Transition Energies on Structure for Single-Walled Carbon Nanotubes in Aqueous Suspension: An Empirical Kataura Plot. *Nano Letters* **3**, 1235-1238 (2003).
25. Milosevic, I., Vukovic, T., Dmitrovic, S. & Damnjanovic, M. Polarized optical absorption in carbon nanotubes: A symmetry-based approach. *Physical Review B* **67**, 165418 (2003).
26. Saito, R., Dresselhaus, G. & Dresselhaus, M.S. Trigonal warping effect of carbon nanotubes. *Phys. Rev. B* **61**, 2981 (2000).
27. Spataru, C.D., Ismail-Beigi, S., Benedict, L.X. & Louie, S.G., Excitonic effects and optical spectra of single-walled carbon nanotubes, *Phys. Rev. Lett.* **92**, 077402 (2004)
28. Hertel, T. & Moos, G. Influence of excited electron lifetimes on the electronic structure of carbon nanotubes. *Chem.Phys. Lett.* **320**, 359 (2000).
29. Goupalov, S.V. Optical transitions in carbon nanotubes. *Physical Review B* **72**, 195403 (2005).
30. Rosencher, E. & Vinter, B. *Optoelectronics*. (Cambridge University Press, Cambridge, UK; 2002).

Figure 1:

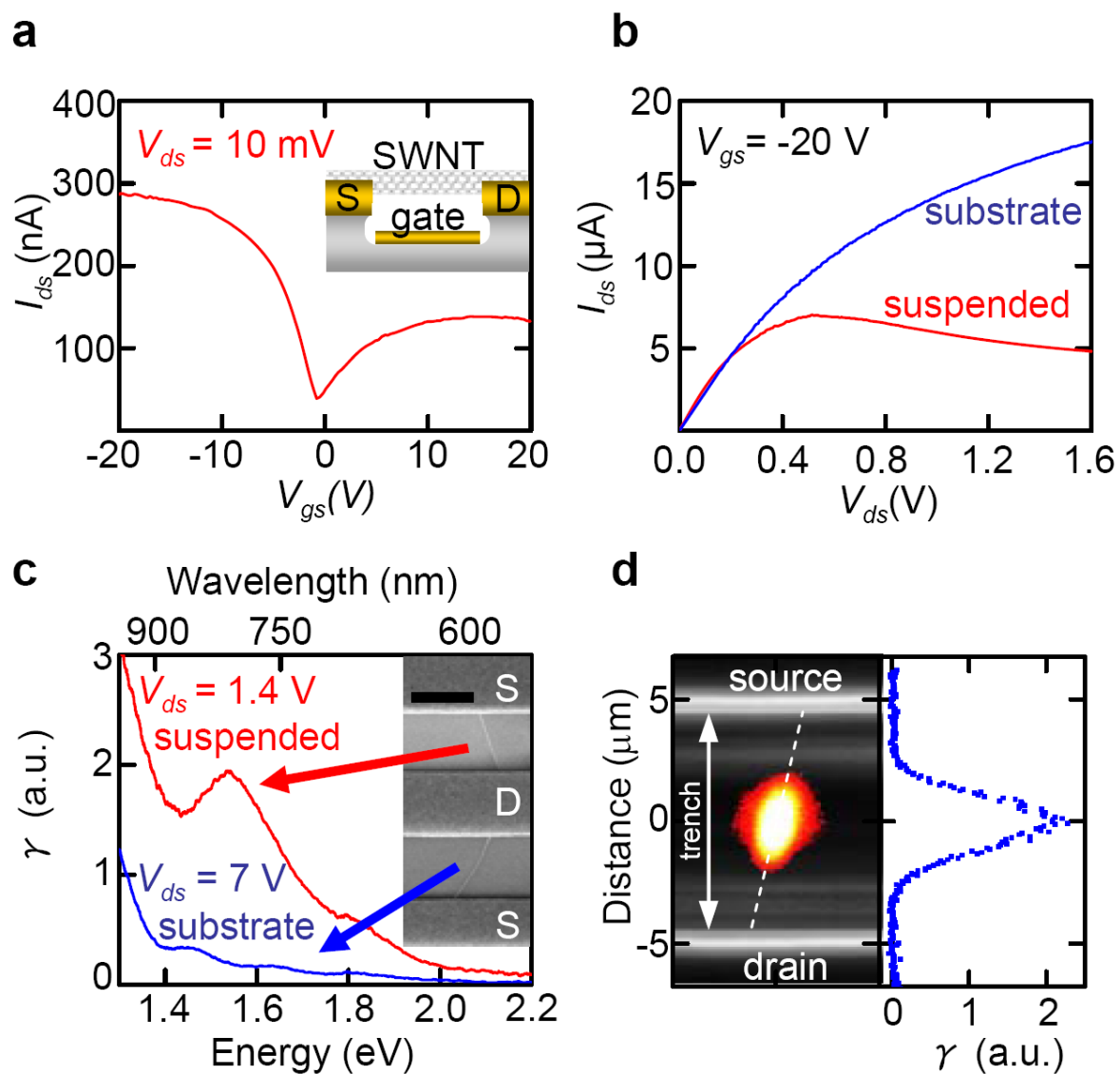


Figure 2:

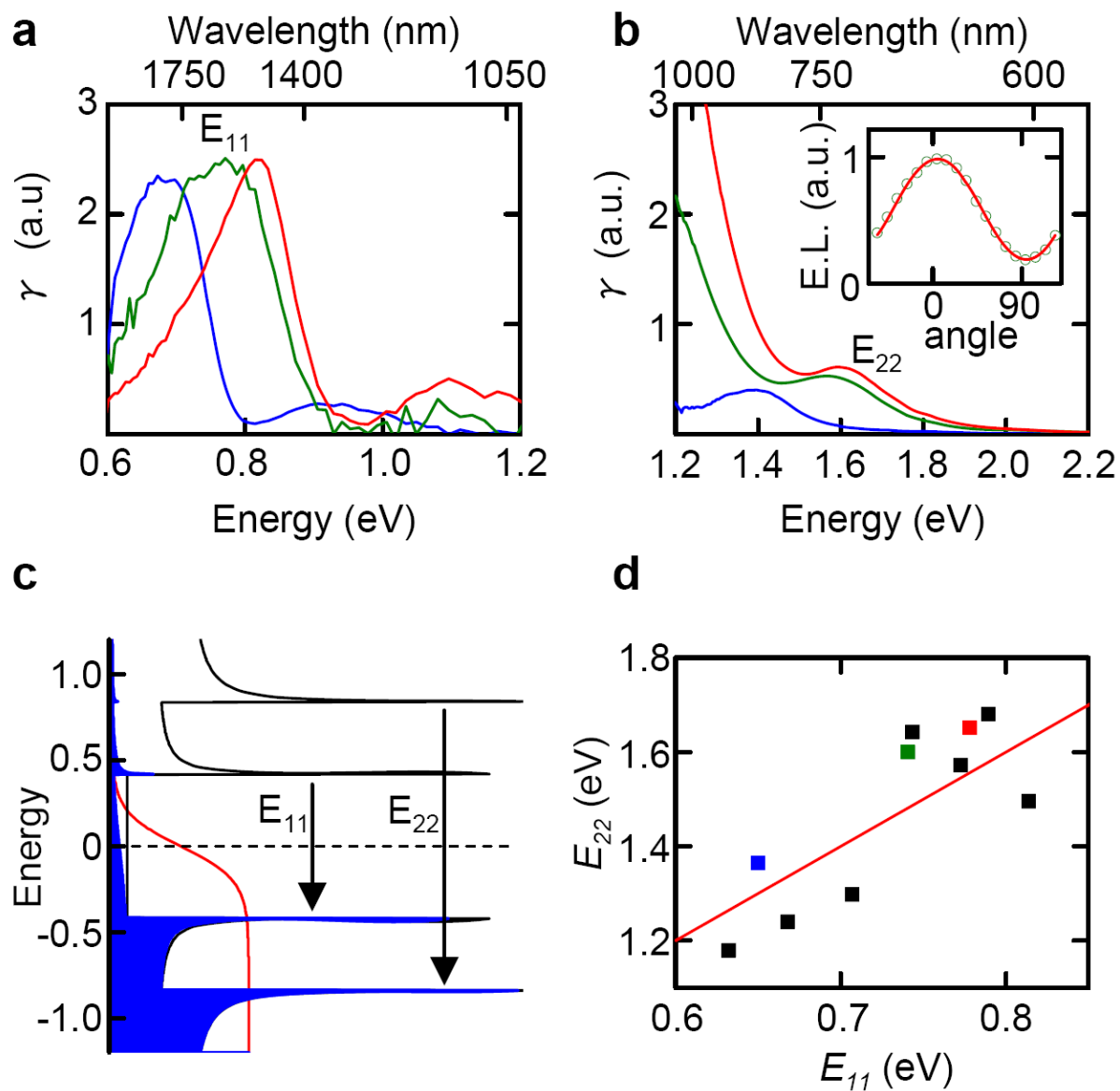


Figure 3:

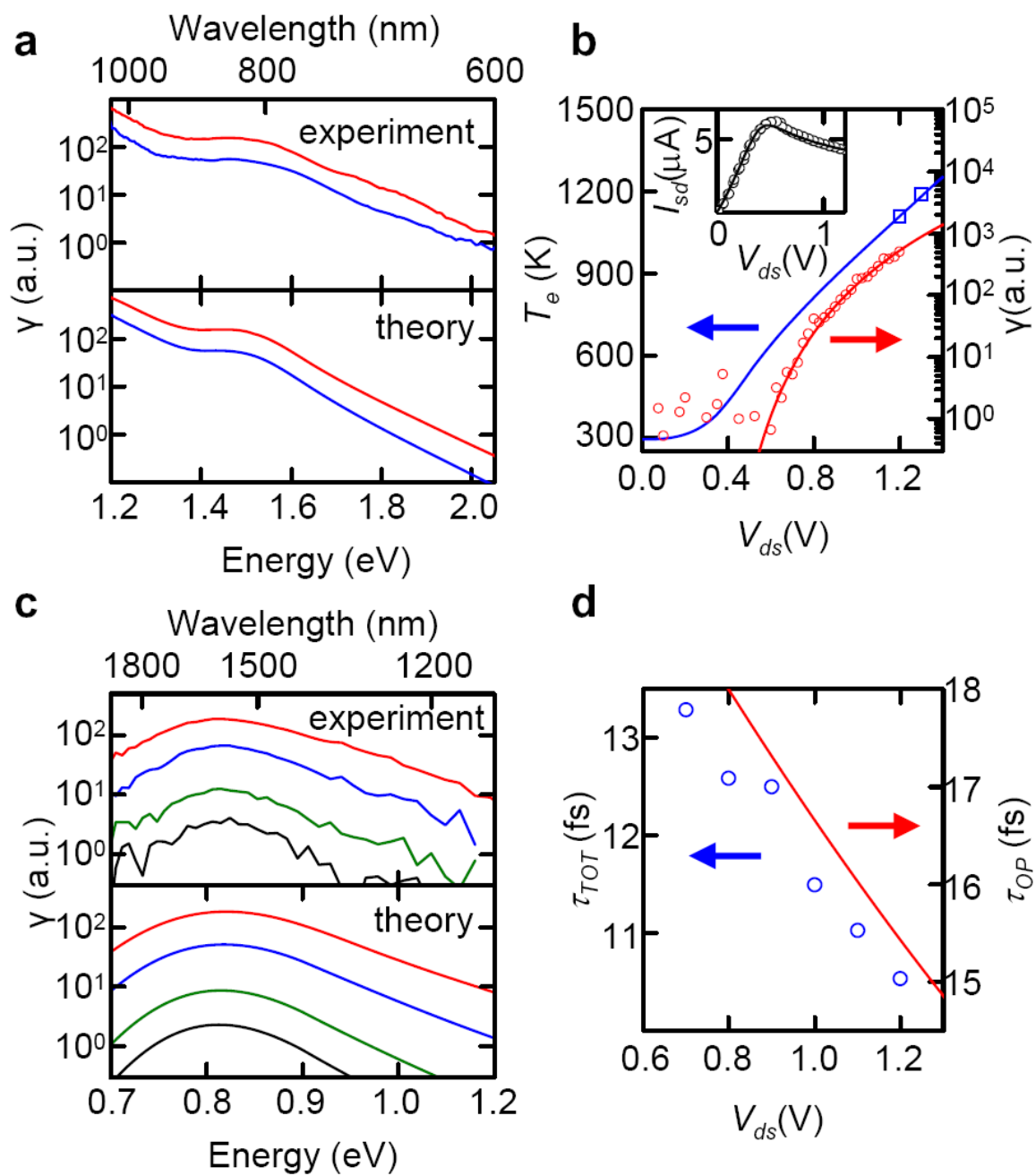
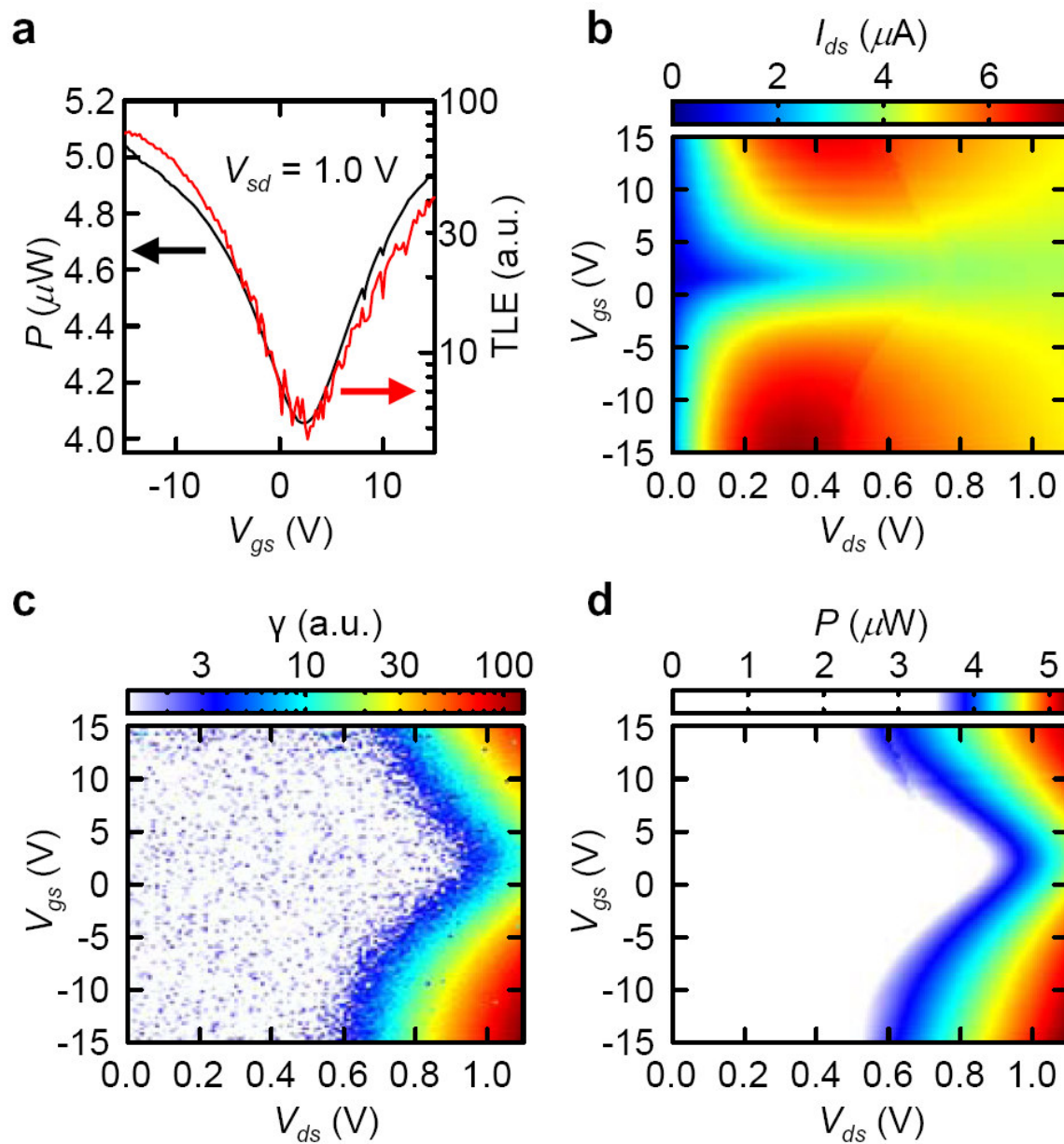


Figure 4:



Supplementary Information.

Experimental Details.

For suspended SWNT devices, we began with photolithographically defined pairs of Pt electrodes spaced 2-10 μm apart (Fig. 1a inset).^{1,2} For “suspended/non-suspended” SWNT chips, we began instead with triplets of Pt electrodes with a trench only between the top and middle electrode.³ (Fig 1c inset) Patterned CVD⁴ growth of SWNTs to bridge the electrodes was performed at 825°C.⁵

Devices were bathed in Argon during measurements to prevent breakdown of the SWNTs by thermal oxidation as a result of joule heating at high V_{ds} .⁶ For thermal light emission (TLE) detection in the visible/near-IR, we used the microscope and detector from a Renishaw micro-Raman spectrometer (with 50X objective lens NA = 0.75). A grating with groove density of 1200 mm^{-1} and thermoelectrically-cooled Silicon CCD array (512×512) (detects $E > 1.2$ eV) were used. For polarization measurements, emitted light passed through a Glan-Thompson polarizer. Typical integration time for spectrum collection was ~60 seconds, though total spectrum collection time was ~20 min due to the high groove density of the grating. For spatially resolved TLE and total emitted light measurements (Fig. 1d), we used a homebuilt scanning confocal microscope (objective lens 80X, NA = 0.8).⁷ Light was collected in a Perkin Elmer SPCM-AQR-15 silicon avalanche photo-diode, sensitive down to 1.2 eV. Collection time for each data point was 10ms. We detected on the order of ~100000 counts/second (efficiency of detection systems was roughly 2%, implying roughly $\sim 5 \times 10^6$ counts/second in the visible/near-IR)

For light detection in the IR, a pair of achromatic lenses were used as an objective (effective NA ~0.6) with a working distance of ~8 mm. The collected light was free-space

coupled with an $f/\#$ of 7 to an imaging Czerny-Turner spectrometer with a focal length of 300 mm. Detection was done with a liquid-nitrogen-cooled InGaAs linear photodiode array (detects $E > 0.58\text{eV}$). A plane ruled grating blazed at 1700 nm with a groove density of 75 mm^{-1} dispersed the light for obtaining spectra, while the total photon counts were measured by using an aluminum mirror to reflect all wavelengths. The $1/f$ noise associated with the large dark current of InGaAs photodiodes was minimized by subtracting background counts at $\sim 0.5\text{ Hz}$, effectively achieving lock-in detection. The spectra were also averaged over all 1024 pixels of the detector to eliminate the effect of response non-uniformity across the array. Typical spectra were collected over 30 min at a resolution of $\sim 17\text{ nm}$. When a mirror is used in place of the grating, typically around 50,000 counts/s (65 photons/count) were detected.

All spectra were corrected for by using the polarization dependent responsivity of both the visible and IR spectrometers. The responsivity was measured by using a Lindberg-Blue tube furnace (with a large graphite crucible at the center) as a blackbody calibration source.

All electrical measurements were performed at room temperature with an Agilent 4156C semiconductor parameter analyzer and an Agilent 33120A arbitrary function generator (for 0.5 Hz pulse generation)

Single Tube Devices.

To ensure that we were measuring single SWNTs in our experiments, we followed a series of standard procedures below.

(1) Catalyst selection: The catalyst we used (Alumina based catalyst) has been shown previously to produce predominately individual tubes of many diameters with very few bundles.⁸ We have used variations on this catalyst (varied to produce different diameter ranges) successfully for many electronic studies on individual SWNTs.^{2, 9-11}

(2) Growth: We aimed to grow a low number of large diameter tubes by tuning the amount and composition of the catalyst, as well as adjusting the growth temperature and conditions. We aimed for approximately 20% yield, meaning 20% of the devices in each growth succeeded in making an electrical connection. At this low yield, it is unlikely to produce bundles, since the total number of tubes produced is so low. Beyond that, we noted that $\sim 2/3$ of the electrically connected devices were semiconductors, which would not be the case if we were measuring bundles.

(3) After growth, we selected devices via electrical probing that were stable, and had peak conduction levels on substrate that did not exceed $25\mu\text{A}$ (indicative of a single tube) under high biases, and also had clear negative differential conductance (NDC) on the suspended portion (multiple tubes or bundles can lead to kinks and irregularities in the NDC). Further, after the emission measurements were concluded, we took several devices and used electrical breakdown in air (breakdown voltage $\sim 1.5\text{-}2.5\text{ V}$ for $\sim 2\mu\text{m}$ long QM-SWNTs) to determine whether there was a single connection or multiple (or bundles) by counting the number of current jumps during breakdown (Fig.S1). Any data that came from a device with multiple connections was discarded, and its characteristics were noted so that we could avoid that type of device in the future ($I_{ds}\text{-}V_{gs}$, $I\text{-}V$ and emission characteristics).

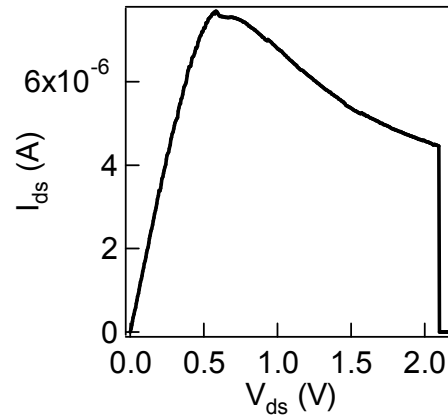


Figure S1: Electrical breakdown of an individual suspended QM-SWNT in air. The sudden current jump to zero at ~ 2 V is due to oxidation of the joule heated nanotube.

The electrical breakdown voltages in air (1.5-2.5V) of our QM-SWNT devices are close to but somewhat higher than the upper bound of bias voltages used in our TLE experiments in Ar. In air, during I-V sweeps, SWNTs can survive brief sweeps to higher voltages than constant holding voltages applied across the tubes continuously. This suggests a QM-SWNT can sustain higher temperature for shorter time against oxidation in air.

TLE of suspended semiconducting SWNTs (S-SWNTs) due to electronic heating.

Fig.S2a shows TLE spectra of a suspended S-SWNT device taken at two biases (V_{ds}) showing a single spectral peak in the IR in the on-state of the device under $V_{gs} = -20$ V. A strong bias dependence of the TLE intensity is seen, similar to the suspended QM-SWNT devices in the main text. Fig.S2b shows a 2-D compilation of many I_{ds} - V_{ds} taken from $V_{gs} = -20$ to 20V for the S-SWNT device. This is a p-channel device, with NDC at $V_{gs} = -20$ V and no current in the $V_{gs} > 0$ region.

Fig.S2c shows TLE (γ) simultaneously collected during I_{ds} - V_{ds} map in Fig. S2b, plotted in log scale. Fig.S2d shows the total power P dissipated over device and contacts plotted in linear scale. For any given V_{gs} , γ scales exponentially with P similar to the device in Figure 4 in the main text for QM-SWNTs. This qualitatively suggests that TLE in suspended S-SWNTs increases as self-heating increases (or as power dissipation increases). In contrast to the QM-SWNT in Figure 4, however, the overall scaling factor for γ to P changes a little as a function of V_{gs} , as a result of significant contact resistance for S-SWNT devices due to Schottky barriers at the contacts.

To understand the small P to γ scaling discrepancy between the QM-SWNT in Figure 4 and the S-SWNT in Figure S2, note first that in both cases the intrinsic contact resistance (R_c) is constant across all V_{gs} , while the SWNT resistance (R_{swnt}) changes with V_{gs} . For the QM-SWNT in Figure 4, R_c is very small compared to the R_{swnt} resistance at high bias ($R_c \sim 15\text{K}\Omega$ vs $R_{swnt} > 150\text{K}\Omega$), which means that for the complete V_{gs} range, the vast majority of the power is dissipated over the SWNT, leading to a simple relationship between total dissipated power and temperature in the SWNT (and thus light emission). In the case of the S-SWNT, R_c is large ($R_c \sim 150\text{K}\Omega$, common for a Pt contacted S-SWNT device). At high bias, R_{swnt} varies from $\sim 150\text{K}\Omega$ at $V_{gs} = -20\text{V}$ to infinity as V_{gs} becomes positive. With $V_{gs} = -20\text{V}$, R_c is on the order of R_{swnt} so a significant part of the total power is dissipated at the contact and does not contribute to SWNT heating. As V_{gs} approaches positive values, $R_{swnt} \gg R_c$, so almost all of the total dissipated power heats the SWNT and thus contributes to light emission. This leads to the observation of more light emission per input power as V_{gs} sweeps from -20V to $+20\text{V}$ in Figure S2c and d.

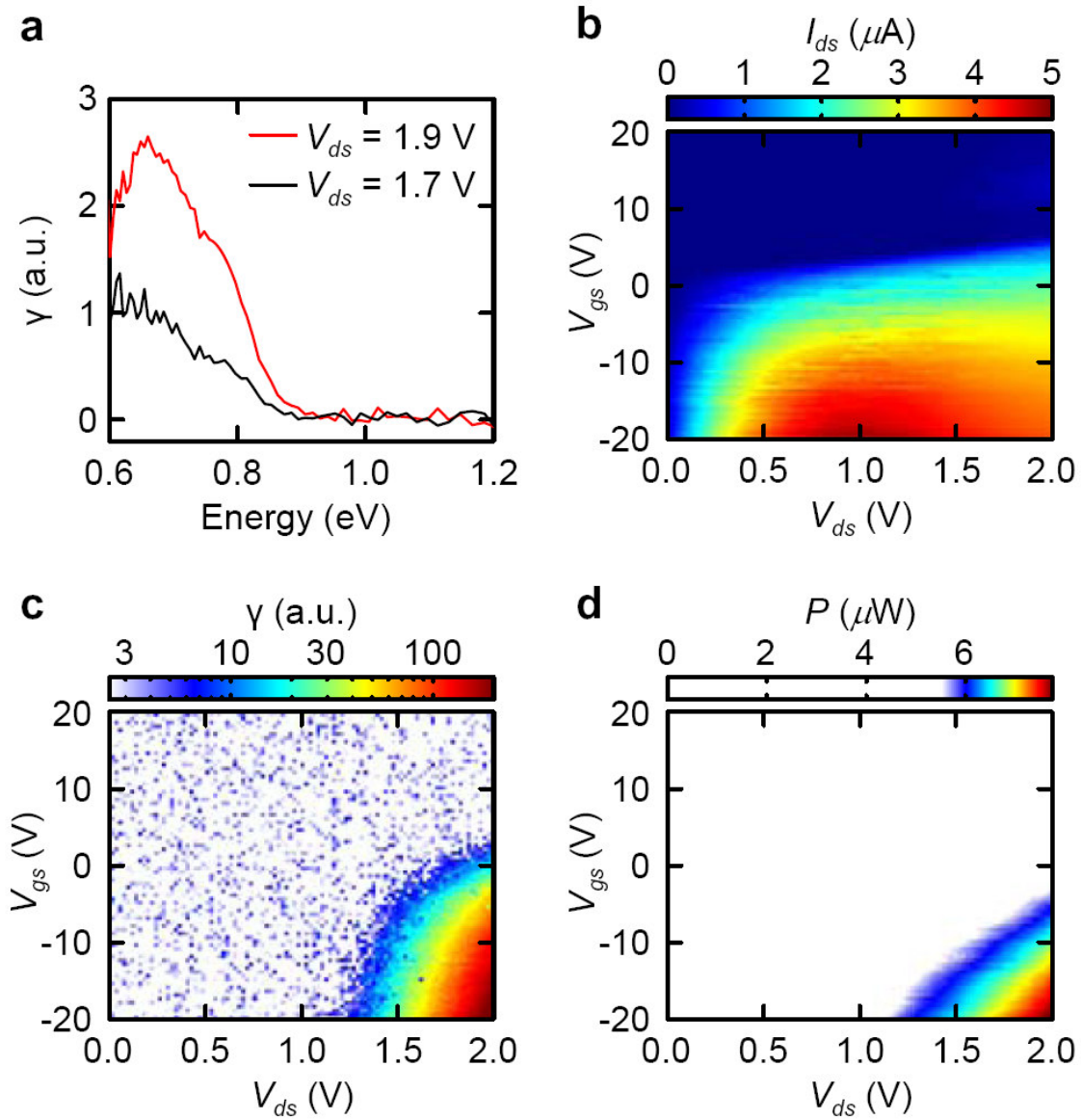


Figure S2: Electrical characteristics and TLE spectra of a semiconducting SWNT device. (a) IR spectra taken at two V_{ds} showing a single spectral peak. (b) A 2-D compilation of many I - V_{ds} taken from $V_{gs} = -20$ to 20. This is a p-channel device, with NDC at $V_{gs} = -20$ V and no current in the $V_{gs} > 0$ region. (c) γ collected during I-V map in Figure S1b, plotted in log scale (d) total P dissipated over device and contacts plotted in linear scale. For any given V_{gs} TLE scales exponentially with P similar to the device in Figure 4. In contrast to Figure 4, the overall scaling factor for TLE to P changes a little as a function of V_{gs} , as a result of significant contact resistance.

References for Supplementary Information:

1. Franklin, N.R., Li, Y., Chen, R.J., Javey, A. & Dai, H. Patterned growth of single-walled carbon nanotubes on full 4-inch wafers. *Appl. Phys. Lett.* **79**, 4571-4573 (2001).
2. Cao, H., Wang, Q., Wang, D.W. & Dai, H.J. Suspended carbon nanotube quantum wires with two gates. *Small* **1**, 138 (2005).
3. Pop, E. et al. Negative differential conductance and hot phonons in suspended nanotube molecular wires. *Phys. Rev. Lett.* **95**, 155505-155508 (2005).
4. Kong, J., Soh, H., Cassell, A., Quate, C.F. & Dai, H. Synthesis of individual single-walled carbon nanotubes on patterned silicon wafers. *Nature* **395**, 878 (1998).
5. Kim, W. et al. Synthesis of ultralong and high percentage of semiconducting single walled carbon nanotubes. *Nano Lett.* **2**, 703-708 (2002).
6. Mann, D. et al. Thermally and molecularly stimulated relaxation of hot phonons in suspended carbon nanotubes. *J. Phys. Chem. B* **110**, 1502-1505 (2006).
7. Fromm, D.P. et al. Exploring the chemical enhancement for surface-enhanced Raman scattering with Au bowtie nanoantennas. *J. Chem. Phys.* **124**, 061101 (2006).
8. Cassell, A., Raymakers, J., Kong, J. & Dai, H. Large scale single-walled nanotubes by CVD synthesis. *J. Phys. Chem.* **103**, 6484-6492 (1999).
9. Cao, J., Wang, Q. & Dai, H. Electron transport in very clean, as-grown suspended carbon nanotubes. *Nat. Mat.* **4**, 745 (2005).
10. Javey, A. et al. High-Field, Quasi-Ballistic Transport in Short Carbon Nanotubes. *Phys. Rev. Lett.* **92**, 106804 (2004).
11. Kong, J. et al. Quantum interference and ballistic transmission in nanotube electron wave-guides. *Phys. Rev. Lett.* **87**, 106801 (2001).